Supplemental Material

Supplemental Material S1: LA-ICP-MS methods and results, additional age-depth modeling methods, and description of modeling code

Supplemental Material S2: LA-ICP-MS data for Hercules I K-bentonite and age-depth model inputs and results

• Table S8: R input data for age-depth modeling of Becker 2020 scale
• Table S9: Age-depth model results: Recalibrated conodont biozones of the Kaufmann scale
• Table S10: Age-depth model results: Recalibrated conodont biozones of the Becker 2012 scale
• Table S11: Age-depth model results: Recalibrated conodont biozones of the Becker 2020 scale

Supplemental Material S3: R script for executing age-depth modeling procedure

Supplemental Material S4: R script for anchoring floating astrochronology durations

SUPPLEMENTAL MATERIAL S1: LA-ICP-MS METHODS AND RESULTS, ADDITIONAL AGE-DEPTH MODELING METHODS, AND DESCRIPTION OF MODELING CODE
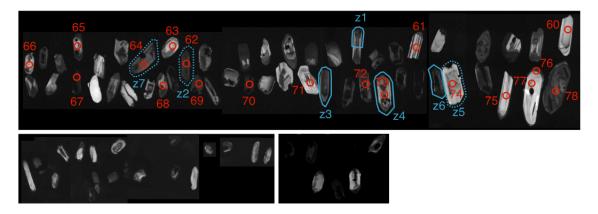
1. Geochronology of the Horologium II K-bentonite

We sampled the Horologium II K-bentonite from the *Polygnathus costatus partitus* zone from the GSSP section in Wetteldorf, Germany (50.14983°N, 006.47135°E, World Geodetic System 1984 [WGS84]; sample: 12VD-83; Figure 1A of main text). We targeted this K-bentonite because of its proximity to the global stratotype section and point (GSSP), but we were unable to determine an age for the associated volcanic event because of significant inheritance and extreme metamictization of U-rich zircon grains. Similarly, Kaufmann et al. (2005) and De Vleeschouwer et al. (2018) document issues with dating the Horologium II K-bentonite.
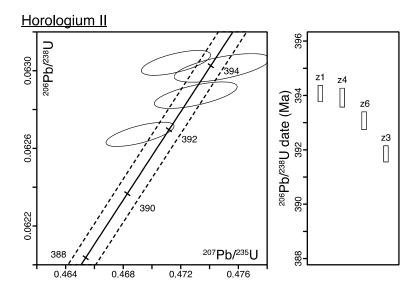
We mounted, polished to grain centers, and imaged 76 Horologium II zircon grains by cathodoluminescence (CL; Fig. S1). The zircon grains in this sample were generally equant and small. Zircon grains were commonly very dark in CL, indicating U-rich grains that were likely to have too much lattice damage to be successfully dated. Also, many grains were too small for dating by in situ laser ablation–inductively coupled plasma–mass spectrometry (LA-ICP-MS) followed by chemical abrasion–isotope dilution–thermal ionization mass spectrometry (CA-ID-TIMS).

We dated 19 spots on 18 Horologium II zircon grains by LA-ICP-MS (methods described below in section 2, results given in Data Repository Item DR2, Table S2). Based on zoning patterns visible in CL images and LA-ICP-MS $^{206}Pb/^{238}U$ dates, we selected seven zircon grains for dating by CA-ID-TIMS. Our CA-ID-TIMS methods for zircon followed those described in the Geochronology Methods section of the main text. We were only able to successfully date four zircon grains because some zircon grains dissolved during chemical abrasion. CA-ID-TIMS dates for the Horologium II K-bentonite ranged from 394.07 ± 0.31 Ma to 391.85 ± 0.31 Ma (Table S4).

We decided not to include the Horologium II K-bentonite in our Devonian time scale compilation because we were not confident in our ability to accurately date the associated volcanic event. About half of the LA-ICP-MS–dated grains yielded dates older than the Devonian Period. Of the zircon grains selected for CA-ID-TIMS that did not dissolve during chemical abrasion, we were unable generate a weighted mean age that we were confident represented the age of the volcanic event and not inheritance or Pb loss. For this work we chose to focus instead on the Hercules I ash bed because of the greater availability of Devonian age, elongate, prismatic grains.

Figure S1. CL grain images and LA-ICP-MS spot locations for zircon from the Horologium II K-bentonite. Red open circles are 25 μm in diameter LA-ICP-MS spots, and the red numbers indicate the LA-ICP-MS spot number. The zircon grains plucked for CA-ID-TIMS work are indicated by blue outlines and a label starting with "z." The solid blue outlines indicate grains successfully dated by CA-ID-TIMS and the dashed blue outlines indicate grains that we attempted to but were unable to date by CA-ID-TIMS.

Figure S2. Concordia diagram (left) and ranked date plot (right) of U-Pb zircon CA-ID-TIMS results for the Horologium II K-bentonite. Error ellipses and error bars are 2σ.

2. LA-ICP-MS analysis

One hundred and sixty-six zircon grains from the Hercules I K-bentonite (sample: 12VD-80) were mounted in epoxy, polished to grain centers, and imaged by cathodoluminescence (CL). Fifty-nine in situ laser ablation–inductively coupled plasma–mass spectrometry (LA-ICP-MS) spots were placed on 47 zircon grains following the methods described in Macdonald et al. (2018) and with analytical parameters described in Table S1 (Supplemental Material S2) to produce preliminary age determinations and trace element concentrations (Tables S2-S3; Supplemental Material S2). Of the 59 LA-ICP-MS spots, only 15 spots had Devonian dates. This is consistent with the inherited cores visible in the CL. The youngest LA-ICP-MS dates and their associated errors are equivalent to the CA-ID-TIMS weighted mean ages for this sample.
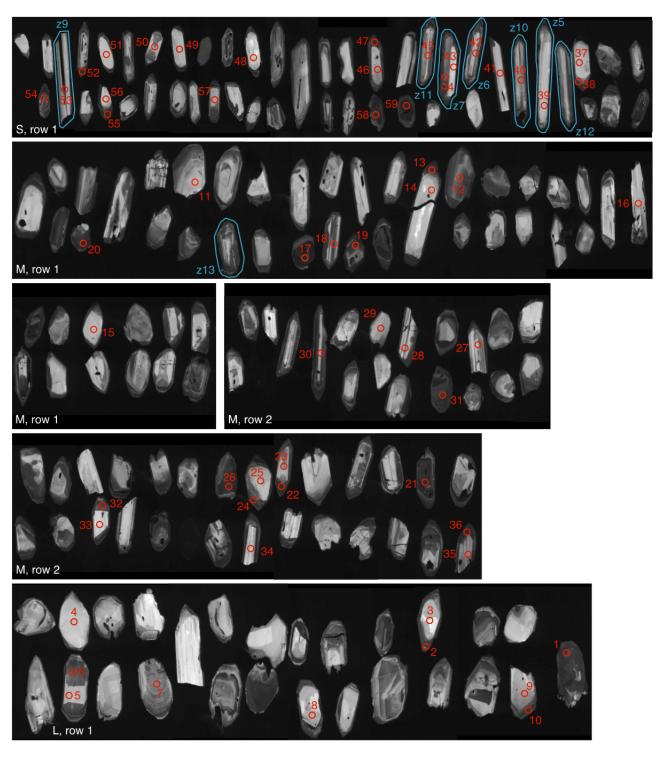
Figure S3. CL grain images and LA-ICP-MS spot locations for zircon from the Hercules I K-bentonite. Red open circles are 25 μm in diameter LA-ICP-MS spots, and the red numbers indicate the LA-ICP-MS spot number. The zircon grains plucked for ID-TIMS work are indicated by a light blue outline and a TIMS label starting with "z."

Figure S4. Probability density plot of LA-ICP-MS U-Pb zircon dates for the Hercules I K-bentonite.

3. Additional age-depth modeling methods

3.1. Sourcing conodont biozonation schemes for age-depth modeling

Our three conodont biozonation schemes used in the age-depth modeling, the Kaufmann, Becker 2012, and Becker 2020 scales, are derived from Kaufmann (2006), Becker et al. (2012), and Becker et al. (2020), respectively. We needed to append additional conodont biozones to the biostratigraphic scales to include Silurian and Carboniferous ages in our modeling. The inclusion of ages outside of the Devonian Period minimizes model uncertainty at the Silurian-Devonian and Devonian-Carboniferous boundaries caused by extrapolating across those boundaries. The Kaufmann scale includes some Carboniferous conodont biozones, making the addition of Carboniferous radioisotopic ages into the model straightforward. We added Carboniferous conodont biozones to the Becker 2012 scale by matching the thickness of the *Siphonodella sulcata* zone in the Carboniferous chapter of the GTS2012 (Fig. 23.5, Davydov et al., 2012) to the thickness of the *S. sulcata* zone on the Becker 2012 scale. We followed the same procedure to append the Carboniferous conodont biozones from the GTS2020 (Fig. 23.7, Aretz et al., 2020) to the Becker 2020 scale, matching the thickness of the *S. sulcata* zone. We added the Pridoli and Ludlow conodont biozones of the Silurian using Figure 9 of McAdams et al. (2017), matching the thickness of the *Ancyrodelloides trigonicus* through the *Caudicriodus postwoschmidti/Caudicriodus hesperius* zones on the Kaufmann scale and the thickness of the *A. trigonicus* through the *C. hesperius* zones between on the Becker 2012 and Becker 2020 scales.

We normalized the *y* axis across the three biostratigraphic scales, assigning a position of 0 to the Silurian-Devonian boundary and a position of 100 to the Devonian-Carboniferous boundary.

3.2. Assignment of relative stratigraphic position to radioisotopic ages

Following the logic described below for each age, we assigned relative stratigraphic positions to the radioisotopic ages and used these ages and positions as input into our age-depth models. Based on which conodont biozone, biozones, or portions of a biozone correspond to each radioisotopic age, we assigned each age a scaled stratigraphic position and uncertainty on each scale, represented by the black rectangles on Figure 3 of the main text. The *y* axis value of the midpoints of the black rectangles in Figure 3 is used as the scaled stratigraphic position, and

the box height, representing uncertainty in the biozone assignment, is used as the uncertainty on those positions. Figure S3 illustrates the radioisotopic ages and uncertainties as probability density functions whose bases are positioned at the assigned scaled stratigraphic position for each age. The uncertainty on the scaled stratigraphic position of each age is represented by a vertical error bar.

We generally favored the conodont biozone assignment of the references that published each radioisotopic age. The text below describes how we translated a conodont biozone assignment from the literature to the Kaufman and Becker 2012 scales. Becker et al. (2020) does the work of assessing the validity of the biozone assignments of the referenced papers. We drew the biostratigraphic assignments for the Becker 2020 scale from the text of Becker et al. (2020); see that text for more detailed explanations of the biostratigraphic assignments. In cases where Becker et al. (2020) assigned an age to a specific but difficult to accurately replicate interval (e.g., age D19 assigned to the "middle part of the *Pa. bogartensis* Zone"), we generally preferred to use a more generous relative stratigraphic assignment, typically spanning the entire conodont zone or zones. Those instances and other clarifications on how we associated radioisotopic ages with the conodont biozones of Becker 2020 scale are noted below.

All biozones listed below are implied to be conodonts unless otherwise specified.

S7: Cramer et al. (2014) dated an ash bed from the Hrynchuk Formation, Podolia, Ukraine at 424.08 ± 0.20(0.29)[0.53] Ma and associated this age to the *Polygnathoides siluricus* zone. We use the *P. siluricus* zone on the Kaufmann, Becker 2012, and Becker 2020 scales as the relative stratigraphic position for the S7 age.

S8: Cramer et al. (2014) dated an ash bed from the Pryhorodok Formation, Podolia, Ukraine at 422.91 ± 0.07(0.21)[0.49] Ma and assigned this age to the *Ozarkodina crispa* zone. Following reassignment of this age described in the Silurian chapter of the GTS2020 (Melchin et al., 2020), we assigned this age to the *O. crispa* zone and the lowermost quarter of the *Ozarkodina eosteinhornensis* sensu lado interval zone on the Kaufmann, Becker 2012, and Becker 2020 scales.

D1-D5, D7: Ages D1 through D5 and D7 from Husson et al. (2016) are a series of bentonites from the Helderberg Group, Cobleskill and Cherry Valley, New York, USA and Smoke Hole, West Virgina, USA with relative position to each other known but with poor biostratigraphic context provided in the paper. The ages range from 418.42 ± 0.21(0.27)[0.53] Ma (D1) to 417.22 ± 0.21(0.23)[0.50] Ma (D7). D5 [sample H1–1 of Husson et al. (2016)] is the same ash bed as D6 [sample CV-2 of McAdams et al. (2017)] described below, therefore we use the biostratigraphic constraints described by McAdams et al. (2017) for samples D1-D5 and D7 on the Kaufmann and Becker 2012 scales, assigning these ages to part of the *Caudicriodus postwoschmidti* zone through the end of the *Ancyrodelloides trigonicus* zone. See below. For the Becker 2020 scale, we assigned these ages to the upper half of the lower Lochkovian.

D6: McAdams et al. (2017) assigned their age of 417.61 ± 0.12(0.23)[0.50] Ma of the Judd Falls metabentonite, Cherry Valley, New York, USA to parts of the *Caudicriodus postwoschmidti* zone, and all of the *Lanea omoalpha*, *Lanea transitans*, *Lanea eleanorae*, and *Ancyrodelloides trigonicus* zones. The Kaufmann alternative scale includes the *L. omoalpha*, *L. eleanorae*, and *A. trigonicus* zones, but lacks the *L. transitans* zone between *L. omoalpha* and *L. eleanorae*. The Kaufmann alternative scale also lacks *C. postwoschmidti* and assigns *Caudicriodus hesperius* to the location occupied by *C. postwoschmidti* on the Kaufmann standard scale. When assigning a position to D6 on the Kaufmann scale, we scaled the McAdams et al. (2017) scale such that the upper boundary of the *A. trigonicus* zone and the lower boundary

of the *C. postwoschmidti/C. hesperius* zones aligned between the McAdams et al. (2017) and Kaufmann alternative scales. The thickness, or uncertainty on the stratigraphic position, of D6 scaled accordingly. For assignment of D6 to the Becker 2012 scale, we similarly aligned the upper boundary of the *A. trigonicus* zone and the lower boundary of the *C. hesperius* zone between the McAdams et al. (2017) and Becker 2012 scales, and the thickness of D6 scaled accordingly. McAdams et al. (2017) notes that the *L. transitans* and *L. eleanorae* zones are reversed on the Becker 2012 scale, and the order in the McAdams et al. (2017) scale is consistent with the order of conodont zones described by Corradini and Corriga (2012). As mentioned above, D6 is the same ash bed as D5, and we use the biostratigraphic constraints on D6 for D1-D5 and D7. For the Becker 2020 scale, we assigned these ages to the upper half of the lower Lochkovian.

  D8: Bodorkos et al. (2017) assigned their age of 417.7 ± 0.5 Ma of the Bulls Camp Volcanics, eastern Australia to the *Caudicriodus woschmidti* through *Eurekadonta eurekaensis* zones. For the Kaufmann scale, assignment of stratigraphic position for modeling was straightforward, and we assigned D8 to span the *C. postwoschmidti/C. woschmidti* and *E. eurekaensis* zones. For the Becker scale, however, the *C. woschmidti* to *E. eurekaensis* zones are not present. The *Caudicriodus hesperius* zone is equivalent to the *C. woschmidti* zone (Carls et al., 2007; Corradini and Corriga, 2012) and the *E. eurekaensis* zone is equivalent to the *C. postwoschmidti*, *Ancyrodelloides carlsi*, and the lower part of the *Ozarkodina delta* (*Lanea omoalpha*) zones (Corradini and Corriga, 2012), so we assigned D8 to span the *C. hesperius* and *L. omoalpha* zones on the Becker 2012 scale. Becker et al. (2020) noted the difficulty in assessing the biostratigraphic age of this volcanic ash bed, associated this age with "much of the lower Lochkovian," and noted that this age is older than the *Ancyrodelloides transitans* zone. Therefore, we assigned D8 to span from the base of the Lochkovian to the base of the *A. transitans* zone on the Becker 2020 scale.

  D9: Bodorkos et al. (2017) assigned their age of 415.6 ± 0.8 of the volcanic Turondale Formation, eastern Australia to the *Eurekadonta eurekaensis* to *Ozarkodina delta* zones. We assigned D9 to span the *E. eurekaensis* and *O. delta* Zones on the Kaufmann scale. We assigned D9 to span from the *C. postwoschmidti* (see explanation for D8 above) to the *A. trigonicus* zones on the Becker 2012 scale because the *O. delta* zone includes *L. omoalpha*, *L. transitans*, *L. eleanorae*, and *A. trigonicus* zones (Corradini and Corriga, 2012). Following the same reasoning as D8, we assigned the D9 age to the base of the Lochkovian through to the base of the *A. transitans* zone on the Becker 2020 scale.

  D10: Parry et al. (2011) associated their Milton of Noth andesite lava flow, Rhynie, Scotland age of 411.5 ± 1.1(1.2)[1.3] Ma to the early (but not earliest) Pragian to earliest Emsian based on *polygonalis-emsiensis* spore assemblages (Wellman, 2004). Becker et al. (2012) charted spore biozones which can be linked to their conodont biozones using the scaling of the Devonian Stages. We assigned D10 to the *Gondwania kindlei* zone through most of *Eocostapolygnathus excavatus* zone on the Becker 2012 scale. For the Kaufmann scale, we assigned D10 to *G. kindlei* through middle *E. excavatus*. For the Becker 2020 scale, the text of Becker et al. (2020) notes that the *polygonalis-emsiensis* spore zone "occupies most of the Pragian" so we have assigned this age to span the entire Pragian.

  D11: Bodorkos et al. (2017) dated three felsic volcanic samples from the Merrions Formation, eastern Australia, at 411.7 ± 0.9 Ma, 413.8 ± 0.8 Ma, and 412.7 ± 1.0 Ma for the Lower, Middle, and Upper Merrions Formation, respectively. The Merrions Formation lacks conodonts but overlying brachiopod and dacryoconarid fossils constrain the formation to likely

be Pragian and likely lower to middle Pragian. The GTS2020 only used the Lower Merrions Formation age from Bodorkos et al. (2017) for D11, 411.7 Ma, and uses an uncertainty of ± 0.9 Ma, consistent with the uncertainty listed in Table 1 of Bodorkos et al. (2017), while the text of Bodorkos et al. (2017) lists an uncertainty of ± 0.8 Ma. We have opted to use the larger uncertainty in our modeling. We followed the GTS2020 in using the Lower Merrions Formation age (411.7 ± 0.9 Ma) and assigned D11 to span the entire Pragian for the Kaufmann, Becker 2012, and Becker 2020 scales.

D12: Kaufmann et al. (2005) dated a volcaniclastic layer from Bundenbach, Germany at 407.7 ± 0.7 Ma and assigned this age to the upper part of the *Polygnathus excavatus* zone. The GTS2012 (Appendix 2, Schmitz, 2012) recalculated the age of concordant analyses as 407.75 ± 1.08(1.33)[1.40] Ma, and we use this age for our modeling. In this case, the recalculated uncertainty of 1.08 Ma includes analytical uncertainty and the uncertainty associated with spike calibration relative to the EARTHTIME tracers. We assigned this age to the upper half of the *P. excavatus* zone on the Kaufmann scale. Kaufmann et al. (2005) also assigned this age to the upper half of the *Polygnathus gronbergi* zone which they explain as equivalent to the *P. excavatus* zone. However, the Becker 2012 scale lists both *Eocostapolygnathus excavatus* and *Eocostapolygnathus gronbergi* zones. Thus, the assignment on the Becker scale is not straightforward, so we have assigned D12 to span the *E. excavatus* and *E. gronbergi* zones on the Becker 2012 scale. Becker et al. (2020) assigned this age to the overlap of the *Nowakia (Dimitriella) praecuror* dracryoconarids zone and the *E. gronbergi* conodont zone, equivalent to approximately the upper half of the *E. gronbergi* conodont zone which is where we assigned this age on the Becker 2020 scale.

D13: Our new age for the Hercules I K-bentonite, Wetteldorf, Germany is 394.290 ± 0.097(0.21)[0.47] Ma. As discussed in the main text, we assigned this age to the upper half of the *Polygnathus costatus patulus* zone on the Kaufmann, Becker 2012, and Becker 2020 scales.

D14: Our new age for the Tioga B K-bentonite, Fayette, New York, USA is 390.82 ± 0.18(0.26)[0.48] Ma. As discussed in the main text, we assigned this age to the upper half of the *Polygnathus costatus costatus* zone on the Kaufmann, Becker 2012, and Becker 2020 scales. The Becker 2020 scale, however, has a dashed boundary at the base of the *Polygnathus pseudofoliatus* zone above the *P.c. costatus* zone. We have extended D14 on the Becker 2020 scale through the *P. pseudofoliatus* zone to account for this uncertainty on the upper bounds of the *P.c. costatus* zone.

D15: Our new age for the Tioga F K-bentonite, Fayette, New York, USA is 390.14 ± 0.14(0.23)[0.47] Ma. As discussed in the main text, we assigned this age to the *Tortodus kockelianus australis* zone and the upper half of the *Polygnathus costatus costatus* zone on the Kaufmann scale. The Becker 2012 scale lacks a *T.k. australis* zone so we assigned this age to the upper half of the *P. c. costatus* zone. We have assigned D15 on the Becker 2020 scale from the base of the *P.c. costatus* zone through the *T.k. australis* zone.

D16: Lanik et al. (2016) dated a tephra layer from the Belpre Tephra Suite, Tennessee, USA at 375.55 ± 0.10(0.21)[0.44] Ma. They associated this age with Frasnian Zones 5–8, which they say is approximately equivalent to the upper part of the lower *Palmatolepis hassi* zone. We assigned this age to Frasnian Zones 5–8 on the Kaufmann alternative scale and the lower half of the *P. hassi* zone on the Becker 2012 scale. For the Becker 2020 scale, we assigned D16 to the *Palmatolepis housei* zone as suggested by Becker et al. (2020).

D17: Lanik et al. (2016) dated a second tephra layer from the Belpre Tephra Suite, Tennessee, USA at 375.25 ± 0.13(0.22)[0.45] Ma. D17 was collected in the same site as D16 and

yields a younger age D16, consistent with D17 being found stratigraphically higher than D16. They assigned age D17 to Frasnian Zone 8, and we use this same assignment on the Kaufmann scale. For the Becker 2012 scale, we assigned this age to the lower half of the *Palmatolepis hassi* zone, the same assignment as D16. For the Becker 2020 scale, we assigned this age to the *Palmatolepis housei* zone, the same assignment as D16.

D18: Lanik et al. (2016) dated a tephra layer from the Rhinestreet Formation, New York, USA at 375.14 ± 0.12(0.22)[0.45] Ma. This age is younger than D17 which is contrary to what Lanik et al. (2016) expected given the biostratigraphic constraints that place this tephra layer in Frasnian Zone 7, a constraint which would make this layer older than D17. They discuss this conflict between the radioisotopic ages and the biostratigraphic constraints and conclude that the zonal boundaries are within the resolution of the uncertainty on the radioisotopic ages. We assigned this age to Frasnian Zone 7 on the Kaufmann scale and the lower half of the *Palmatolepis hassi* zone on the Becker 2012 scale. For the Becker 2020 scale, we assigned D18 to the *"Ozarkodina" nonaginta* zone as suggested by Becker et al. (2020).

D19: Percival et al. (2018) dated a bentonite from Kellerwald, Germany at 372.360 ± 0.053(0.11)[0.41] Ma and assigned this age to the late *Palmatolepis rhenana* zone. We assigned this age to the upper *P. rhenana* zone of the Kaufmann scale and the upper half of the *P. rhenana* zone of the Becker 2012 scale. Becker et al. (2020) correlated this age with the middle part of the *Palmatolepis bogartensis* zone, and we assigned this age to all of the *P. bogartensis* zone.

D20–21: We omitted the Re-Os ages of black shales by Turgeon et al. (2007) and restricted this modeling to U-Pb ages to eliminate decay constant uncertainty.

D22: Tucker et al. (1998) dated a pumiceous tuff from the Carrow Formation, New Brunswick, Canada at 363.8 ± 2.2 Ma (weighted mean ^{207}Pb/^{206}Pb age) and assigned the Carrow Formation to the upper *Palmatolepis gracilis expansa* zone. The GTS2012 (Appendix 2, Schmitz, 2012) recalculated the ^{206}Pb/^{238}U age as 364.08 ± 2.05(2.17)[2.20] Ma, and we used this age for our modeling. In this case, the recalculated uncertainty of 2.05 Ma includes analytical uncertainty and the uncertainty associated with spike calibration relative to the EARTHTIME tracers. We assigned this age to the upper *Pa. g. expansa* zone on the Kaufmann scale and the upper half of the *Pa. g. expansa* zone on the Becker 2012 scale. Becker et al. (2020) assigned this age to the "middle to upper parts of the *Bi. costatus* Subzone" and we assigned this age to the entire *Bispathodus costatus* zone on the Becker 2020 scale to mitigate uncertainty in where the middle part of the *Bi. costatus* zone begins on the Becker 2020 scale.

D23: Tucker et al. (1998) dated the Bailey Rock Rhyolite, which intrudes and/or overlies the Carrow Formation, New Brunswick, Canada, at 363.4 ± 1.8 Ma. They associated the Carrow Formation and this age with the upper *Palmatolepis gracilis expansa* zone. The GTS2012 (Appendix 2, Schmitz, 2012) recalculated the ^{206}Pb/^{238}U age as 362.87 ± 0.53(0.88)[0.96] Ma, and we use this age for our modeling. In this case, the recalculated uncertainty of 0.53 Ma includes analytical uncertainty and the uncertainty associated with spike calibration relative to the EARTHTIME tracers. We assigned this age to the upper *Pa. g. expansa* zone on the Kaufmann scale and the upper half of the *Pa. g. expansa* zone on the Becker 2012 scale. Following the same reasoning as the assignment for D22, we assigned D23 to all of the *Bispathodus costatus* zone on the Becker 2020 scale.

D24: We omitted the Re-Os ages of a black shale by Selby and Creaser (2005) and restricted this modeling to U-Pb ages to eliminate decay constant uncertainty.

D25: Davydov et al. (2011) dated an ash bed from the Wocklum Limestone, Rhenish Mountains, Germany at 359.25 ± 0.06(0.18)[0.42] Ma. They assigned this age to the upper
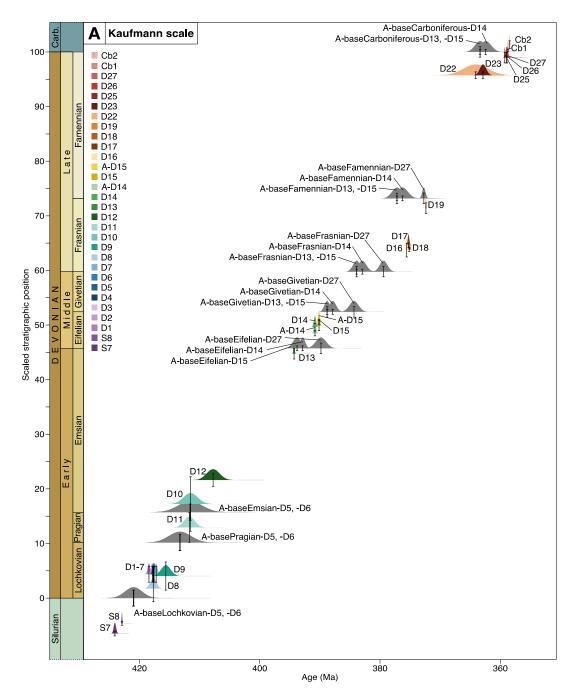
Siphonodella praesulcata zone. We assigned this age to the middle to upper *S. praesulcata* zone on the Kaufmann scale and the entire *S. praesulcata* zone of the Becker 2012 scale. The biostratigraphic assignment for D25 is not discussed in the text of Becker et al. (2020), so we assigned this age to the entire *S. praesulcata* zone of the Becker 2020 scale for consistency with how we assign this age on the Becker 2012 scale.

D26: Myrow et al. (2014) dated an ash bed from the Woclumeria Limestone, Kielce, Poland at $358.97 \pm 0.11(0.19)[0.43]$ Ma and assigned this age to the middle *Palmatolepis gracilis expansa* to late *Siphonodella praesulcata* zones. The location of the ash bed in the stratigraphic section (Fig. 1–2, Myrow et al., 2014) relative to the conodont biozones in Figure 1 of Myrow et al. (2014) suggests a position in the middle to upper *S. praesulcata* zone, so we assigned this age to the middle to upper *S. praesulcata* zone on the Kaufmann scale and the entire *S. praesulcata* zone on the Becker 2012 scale. Becker et al. (2020) assigned this age to the upper part of the *Siphonodella (Eosiphonodella) praesulcata* conodont zone and the *Wocklumeria sphaeroides* ammonoid zone, so we assigned this age to the upper half of the *S. praesulcata* zone of the Becker 2020 scale.
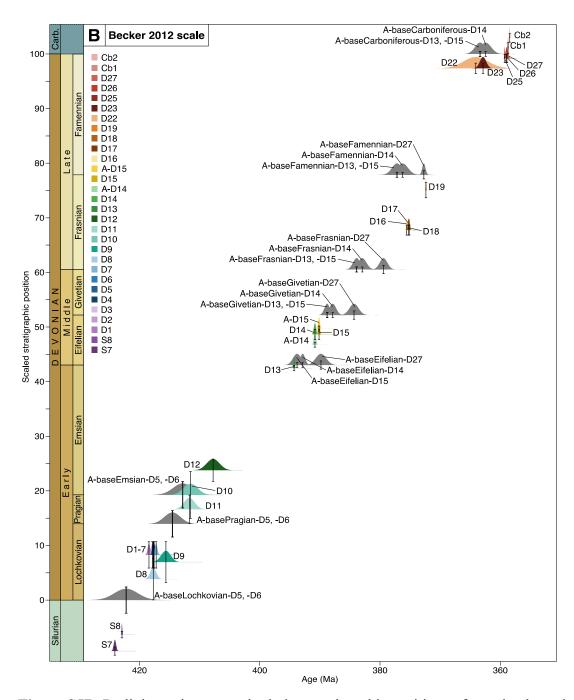
D27: Myrow et al. (2014) dated an ash bed from the Hangenberg Limestone, Kielce, Poland at $358.89 \pm 0.20(0.29)[0.48]$ Ma and assigned this age to the middle *Palmatolepis gracilis expansa* to late *Siphonodella praesulcata* zones. Following the same reasoning as with age D26, we assigned this age to the middle to upper *S. praesulcata* zone on the Kaufmann scale and the entire *S. praesulcata* zone of the Becker 2012 scale. Becker et al. (2020) assigned this age to the middle/upper *Bispathodus costatus – Protognathodus kockeli* interregnum, and we assigned this age to all of the *Bi. costatus – P. kockeli* interregnum on the Becker 2020 scale.

Cb1: Davydov et al. (2011) dated an ash bed, Bed 79 from the Hangenberg Limestone, Rhenish Mountains, Germany, at $358.71 \pm 0.06(0.19)[0.42]$ Ma and assigned this age to the upper *Siphonodella sulcata* zone. We assigned this age to the *S. sulcata* zone on the Kaufmann, Becker 2012, and Becker 2020 scales.
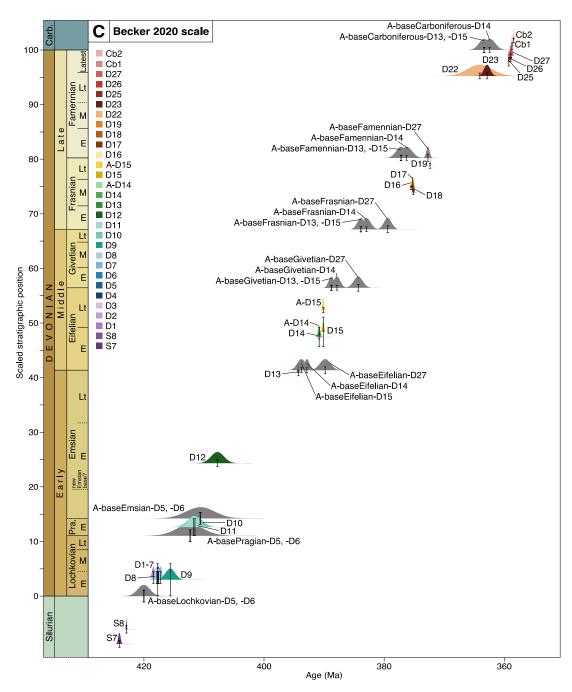
Cb2: Davydov et al. (2011) dated an ash bed, Bed 15 from the Hangenberg Limestone, Rhenish Mountains, Germany, at $358.43 \pm 0.06(0.19)[0.42]$ Ma and assigned this age to the lower *Siphonodella duplicata* zone. We assigned this age to the lower *S. duplicata* zone on the Kaufmann and Becker 2020 scales and the lower half of the *S. duplicata* zone on the Becker 2012 scale.

Figure S5A. Radioisotopic ages and relative stratigraphic positions of age-depth model inputs based on the Kaufmann scale. The colored probability density functions illustrate the radioisotopic age constraints. The dark gray probability density functions illustrate the anchored and extrapolated astrochronologic constraints for the model, described below in Section 3.3. The vertical error bars show the scaled stratigraphic uncertainty associated with each age constraint.

Figure S5B. Radioisotopic ages and relative stratigraphic positions of age-depth model inputs based on the Becker 2012 scale. See caption to Fig. S5A for more detail.

Figure S5C. Radioisotopic ages and relative stratigraphic positions of age-depth model inputs based on the Becker 2020 scale. See caption to Fig. S5A for more detail.

3.3. Astrochronologic constraints for model

The process of incorporating floating astrochronology stage durations into the age-depth models involves anchoring the floating durations on radioisotopic ages. We used astrochronology duration estimates for entire stages (studies described below), revised the uncertainties as necessary to include cycle counting error and stratigraphic uncertainty, and combined durations and uncertainties together when multiple durations were available for a single stage (Famennian, Givetian, and Eifelian Stages; see the main text for equations used to combine durations and uncertainties). It would be possible to create astrochronology model inputs based on individual stage durations, rather than combined durations, or model inputs based on astrochronology durations less than the length of a stage, but we opted to use one combined duration for each stage to allow us to focus on the effect of how the durations are anchored and chained together rather than the variations in different astrochronology studies. In one case, however, we used a duration from an individual study (Eifelian Stage; Pas et al., 2021) because we had radioisotopic ages (D14, D15) from the same section as the cyclostratigraphy work and could thus anchor the astrochronology directly on K-bentonites from the same section. We linked combined stage durations (Table 4) to some of the radioisotopic ages described in the previous section (D5, D6, D13, D27)). These anchors allowed us to extrapolate up or down through the Devonian to create 26 astrochronology inputs for the age-depth model (Fig. S5).

In the anchoring process, we summed Gaussian distributions of radioisotopic ages and uniform distributions of astrochronology durations to extrapolate to the stage boundary of interest. We used the mean and standard deviation of the resulting summed distribution as the stage boundary age. When the anchoring age fell within a stage, we proportionally divided the astrochronology duration and uncertainty according to the relative stratigraphic position within the stage. For example, if an anchoring age was located one-third of the way up from the base of a stage, one-third of the duration and uncertainty would be allocated to the stage below the midpoint of the anchoring age and two-thirds of the duration and uncertainty would be allocated to the stage above the midpoint of the anchoring age. To extrapolate up or down the time scale, we took the summed distribution for a stage boundary and added the uniform distribution of the next astrochronology duration up or down the time scale. Again, we used the mean and standard deviation of the new summed distribution as the age of the next stage boundary. Using the mean and standard deviation of the summed distribution assumes a normal distribution which was generally a good approximation for the summed distributions, particularly as the extrapolation processes added more distributions together. See Fig. S4 for a graphical explanation of this process on anchor D14 and Fig. S5-S6 for documentation of how this process was done for anchors D15, D5, and D6.

Lochkovian: Da Silva et al. (2016) determined the duration of the Lochkovian Stage to be 7.7 ± 2.8 Myr using records from the Czech Republic of magnetic susceptibility and gamma ray spectrometry analyzed by multiple spectral analysis and statistical techniques. They relied on the 405 k.y. eccentricity metronome to determine the duration of the stage. Their uncertainty of 2.8 Myr describes the uncertainty in cycle counting in the section and the uncertainty in the location of the Lochkovian boundaries in the formation studied. We did not revise this uncertainty estimate because it included at least one cycle counting error as well as stratigraphic uncertainty.

Pragian: Da Silva et al. (2016) determined the duration of the Pragian Stage to be 1.7 ± 0.7 Myr using records from the Czech Republic of magnetic susceptibility and gamma ray spectrometry analyzed by multiple spectral analysis and statistical techniques. As with their

Lochkovian work, they used the 405 k.y. eccentricity metronome to determine the duration of the Pragian, and their uncertainty describes uncertainty in cycle counting and in the location of the boundaries of the formation studied. We did not revise this uncertainty estimate because it included at least one cycle counting error as well as stratigraphic uncertainty.

Emsian: To our knowledge, there is no cyclostratigraphic study on the duration of the Emsian.

Eifelian: Ellwood et al. (2015) determined the Eifelian Stage to be 6.28 Myr long and did not report an uncertainty. Their study used magnetic susceptibility records from Morocco to identity signals of the 405 k.y. eccentricity cycle. We estimate uncertainty to be ± 1.00 Myr, composed of two 405 k.y. cycle counting errors and two 200 k.y. uncertainties to account for stratigraphic uncertainty on stage boundaries.

Pas et al. (2021) determined the duration of the Eifelian Stage to be 5 Myr using the 100 k.y. eccentricity cycle. They did not report a numerical value that represents all of the uncertainty on their reported Eifelian duration, noting that uncertainty in the duration can be due to stratigraphic uncertainty on the position of the Eifelian boundaries, cycle counting uncertainty, the use of an artificial signal representing areas where ash bed data has been omitted, and uncertainty due to differences in the results from tuning versus the average spectral misfit technique. To account for these uncertainties in the age-depth model, we assigned a numerical value for the uncertainty of the Eifelian duration of ± 0.80 Myr. We arrived at this uncertainty by adding one 405 k.y. cycle counting error and two 200 k.y. uncertainties to account for stratigraphic uncertainty on stage boundaries.

The section that Pas et al. (2021) sampled at the Seneca Stone Quarry east of Fayette, New York is the same section from which we sampled the Tioga F (D15) and Tioga B (D14; referred to as the Onondaga Indian Nation bentonite by Pas et al. (2021)) ash beds. We used D14 and D15 as points on which to anchor the floating duration of Pas et al. (2021). We used our radioisotopic ages for D14 and D15 and the position within the stage according to Pas et al. (2021) to create A-D14 and A-D15 as model inputs.

Our combined duration and uncertainty for the Eifelian is 5.50 ± 0.39 Myr, computed using Equations 1 and 2 of the main text.

Givetian: With no radioisotopic ages available for the Givetian, astrochronology provides a useful constraint on the duration of the Givetian Stage.

House (1995) estimated the duration of the Givetian at 6.5 Myr based on a section in France with microcyclicity caused by precession. With no uncertainty provided, we use an arbitrary 30% uncertainty (±1.95 Myr) on the duration to account for counting errors and uncertainty on the precession period.

Ellwood et al. (2011) used a model of the 405 k.y. eccentricity cycle in the Givetian, tested against and refined by magnetic susceptibility records from sections in France, Morocco, and the eastern United States, to determine a 5.6 Myr duration for the Givetian. They did not report a numerical uncertainty value, so we estimate uncertainty to be ± 1.10 Myr, composed of two 405 k.y. cycle counting errors and three 200 k.y. uncertainties to account for the stratigraphic uncertainty in the composite construction.

De Vleeschouwer et al. (2014) used the 405 k.y. eccentricity cycle in magnetic susceptibility records of Belgium sections to determine a duration of the Givetian Stage of 4.35 ± 0.45 Myr. The 0.45 Myr uncertainty is due to stratigraphic uncertainty in the stage boundaries and cycle counting uncertainty, and we revised this uncertainty to ± 0.75 Myr based on an

additional three 100 k.y. uncertainties to account for the stratigraphic uncertainty in the composite construction.

Our combined duration and uncertainty for the Givetian is 4.91 ± 0.35 Myr, computed using Equations 1 and 2 of the main text.

Frasnian: De Vleeschouwer et al. (2012) determined the duration of the Frasnian to be 6.5 ± 0.4 Myr based on 405 k.y. eccentricity cycles in magnetic susceptibility data from Alberta, Canada. The uncertainty on this duration is based on one cycle counting error, and the stratigraphic uncertainty of the stage boundaries is assumed to be small and encompassed by the cycling counting uncertainty of 0.405 Myr. Whalen et al. (2016) revised the duration of the Frasnian to 6.7 Myr after reassessing the De Vleeschouwer et al. (2012) magnetic susceptibility data from Alberta, Canada, adding a half cycle of the 405 k.y. eccentricity cycle. We revised the uncertainty to be ± 0.50 Myr by adding one 100 k.y. uncertainty to account for stratigraphic uncertainty on stage boundaries, resulting in a revised duration and uncertainty for the Frasnian of 6.7 ± 0.50 Myr.

Famennian: Pas et al. (2018) determined the duration of the Famennian to be 13.5 ± 0.5 Myr based on magnetic susceptibility records from three cores from the Illinois Basin, United States, analyzed with multiple spectral techniques and tuned to the 405 k.y. eccentricity cycle or the 34.4 k.y. obliquity cycle, depending on the core analyzed. We did not revise this uncertainty estimate because it included at least one cycle counting error as well as stratigraphic uncertainty.

Ma et al. (2020) determined the duration of the Famennian to be 14.4 ± 0.28 Myr based on the spectral analysis of the 405 k.y. eccentricity cycle in the calcium concentration of rocks from a continuous section in Lali, China. The uncertainty on their duration is based on stratigraphic uncertainty on stage boundaries. We revised this uncertainty to ± 0.68 Myr by adding one 405 k.y. counting error.

We combined the durations from Pas et al. (2018) and Ma et al. (2020) using a weighted average and a harmonic sum of revised uncertainties (see Equations 1 and 2 in the main text) and used a combined duration for the Famennian of 13.82 ± 0.16 Myr in our models.
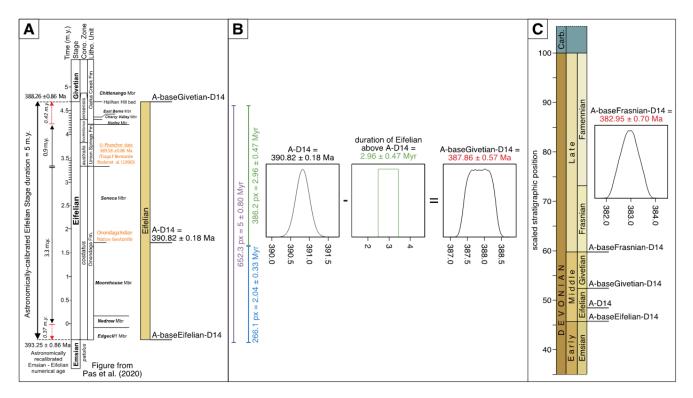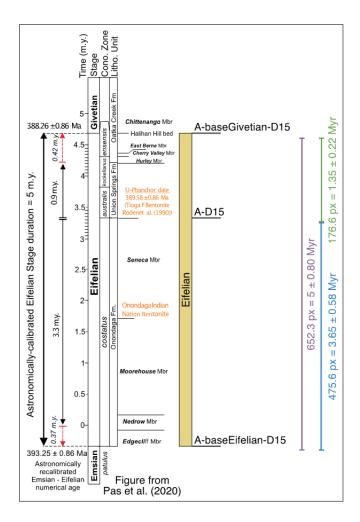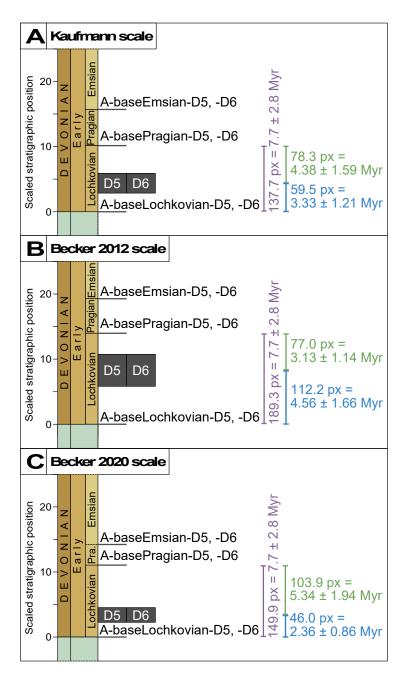
Figure S6. Graphical example of method for anchoring and extrapolating astrochronologic constraints. (A) We noted the location of the marker bed (Onondaga Indian Nation Bentonite = D14) and the base and top of the section relative to the stratigraphic thickness of the Eifelian section from Pas et al. (2021). We paired the D14 radioisotopic age with the relative stratigraphic position of the D14 ash bed within the Eifelian section as measured by Pas et al. (2021) to create model input A-D14. (B) We sampled the normally distributed A-D14 radioisotopic age and the uniformly distributed astrochronology duration to extrapolate to the next position of interest. For example, to determine the age and uncertainty of A-baseGivetian-D14, we first determined the proportion of the stratigraphic thickness between ash bed A-D14 and the base of the Givetian relative to the thickness of the Eifelian section. We used this proportion as a proxy to estimate how much time in the astrochronology-determined Eifelian duration is likely associated with the time between the A-D14 ash bed and the base of the Givetian. In this example, A-D14 and A-baseGivetian-D14 are separated by 386.2 pixels in our graphics software, and that equates to 2.96 Myr if the stage is 5 Myr long and 652.3 pixels tall. We proportionally distributed the astrochronologic uncertainty in the same way. We sampled a normal distribution of the radioisotopic age of A-D14 and subtracted from it the uniform distribution representing the astrochronology duration of the proportion of the Eifelian between A-D14 and A-baseGivetian-D14. This gave us a distribution for A-baseGivetian-D14 from which we extracted mean and two standard deviation values which can be used to approximate a normal distribution in the age-depth model. (C) We continued adding (or subtracting) distributions to determine the age of other stage boundaries. For example, our combined duration for the Givetian is 4.91 ± 0.35 Myr (Table 4, main text), so we subtracted this from the age distribution of A-baseGivetian-D14 to determine an age and uncertainty for A-baseFrasnian-D14.

Figure S7. Following the same method described in Fig. S6, we proportioned the astrochronology duration and uncertainty for the Eifelian based on the location of A-D15, the model input corresponding to the age of D15 and the stratigraphic position within the section measured by Pas et al. (2021).

Figure S8. Following the same method described in Fig. S6, we proportioned the astrochronology duration and uncertainty for the Lochkovian based on the stratigraphic positions of D5 and D6 on each of the three scales.

4. Description of code

The astrochronology extrapolations and age-depth modeling was done in R (R Core Team, 2021), and the scripts are available as additional supplemental material (Supplemental Material S3 and S4) and on GitHub (https://github.com/cohgeo/DevonianAgeDepthModel).

Supplemental Material S4 is an R script used to anchor astrochronology durations to determine the astrochronologic age of stage boundaries used in the age-depth modeling. The .csv files used as input in that script are available on GitHub and summarized in Table S4 (Supplemental Material S2). The results of anchoring the floating astrochronology durations are provided in Table S5 (Supplemental Material S2).

Supplemental Material S3 is an R script that runs an age-depth model on Devonian radioisotopic and anchored astrochronologic ages and their associated relative stratigraphic positions to predict the age of Devonian stage boundaries and the ages of conodont biozones boundaries. The .csv files used as input in that script are available on GitHub and summarized in Tables S6-S8 (Supplemental Material S2).

Running the age-depth model script (Supplemental Material S3) results in recalibrated stage and conodont biozone boundary ages and scaled stratigraphic positions for each scale. Because this procedure relies on a probabilistic model, the model results will vary slightly each time the model is run, even with the same starting parameters and data. Since the model highest density interval and 95% confidence interval will vary slightly between model runs, the linearization process will result in slightly different final stage and conodont biozone boundary scaled stratigraphic positions. We have provided the conodont biozone model results in Tables S9-S11 (Supplemental Material S2) with the caveat that these are one possible model outcome and running the code again could produce slight differences in the predicted ages and scaled stratigraphic positions. In sensitivity tests, we found that stage and conodont biozone boundary positions typically varied by an average of ~0.07 scaled stratigraphic position units (where 0 = the position of the base of the Devonian and 100 = the position of the base of the Carboniferous), and ages varied by an average of ~0.03 Ma.

5. REFERENCES CITED

Aretz, M., Herbig, H.G., Wang, X.D., Gradstein, F.M., Agterberg, F.P., and Ogg, J.G., 2020, Chapter 23 – The Carboniferous Period, *in* Gradstein, F.M., Ogg, J.G., Schmitz, M.D., and Ogg, G.M., eds., Geologic Time Scale 2020: Amsterdam, Netherlands, Elsevier, p. 811–874, https://doi.org/10.1016/B978-0-12-824360-2.00023-1.

Becker, R.T., Gradstein, F.M., and Hammer, O., 2012, Chapter 22 – The Devonian Period, *in* Gradstein, F.M., Ogg, J.G., Schmitz, M.D., and Ogg, G.M., eds., The Geologic Time Scale 2012: Amsterdam, Netherlands, Elsevier BV, p. 559–601, https://doi.org/10.1016/B978-0-444-59425-9.00022-6.

Becker, R.T., Marshall, J.E.A., Da Silva, A.-C., Agterberg, F.P., Gradstein, F.M., and Ogg, J.G., 2020, Chapter 22 – The Devonian Period, *in* Gradstein, F.M., Ogg, J.G., Schmitz, M.D., and Ogg, G.M., eds., Geologic Time Scale 2020: Amsterdam, Netherlands, Elsevier, p. 733–810, https://doi.org/10.1016/B978-0-12-824360-2.00022-X.

Black, L.P., et al., 2004, Improved $^{206}Pb/^{238}U$ microprobe geochronology by the monitoring of a trace-element-related matrix effect; SHRIMP, ID–TIMS, ELA–ICP–MS and oxygen isotope

documentation for a series of zircon standards: Chemical Geology, v. 205, p. 115–140, https://doi.org/10.1016/j.chemgeo.2004.01.003.

Bodorkos, S., Pogson, D., and Friedman, R., 2017, Zircon U-Pb dating of biostratigraphically constrained felsic volcanism in the Lachlan Orogen via SHRIMP and CA-IDTIMS: implications for the division of Early Devonian time [abs.], *in* Vearncombe, J., ed., Bulletin No. 65: Granites2017@Benalla: Australia, Australian Institute of Geoscientists, p. 11–14.

Carls, P., Slavík, L., and Valenzuela-Ríos, J.I., 2007, Revisions of conodont biostratigraphy across the Silurian-Devonian boundary: Bulletin of Geosciences, v. 82, p. 145–164, https://doi.org/10.3140/bull.geosci.2007.02.145.

Corradini, C., and Corriga, M.G., 2012, A Přídolí–Lochkovian conodont zonation in Sardinia and the Carnic Alps: implications for a global zonation scheme: Bulletin of Geosciences, v. 87, p. 635–650, https://doi.org/10.3140/bull.geosci.1304.

Cramer, B.D., Schmitz, M.D., Huff, W.D., and Bergström, S.M., 2014, High-precision U–Pb zircon age constraints on the duration of rapid biogeochemical events during the Ludlow Epoch (Silurian Period): Journal of the Geological Society, v. 172, p. 157–160, https://doi.org/10.1144/jgs2014-094.

Da Silva, A.-C., Hladil, J., Chadimová, L., Slavík, L., Hilgen, F.J., Bábek, O., and Dekkers, M.J., 2016, Refining the Early Devonian time scale using Milankovitch cyclicity in Lochkovian–Pragian sediments (Prague Synform, Czech Republic): Earth and Planetary Science Letters, v. 455, p. 125–139, https://doi.org/10.1016/j.epsl.2016.09.009.

Davydov, V.I., Korn, D., and Schmitz, M.D., 2012, Chapter 23 - The Carboniferous Period, *in* Gradstein, F.M., Ogg, J.G., Schmitz, M.D., and Ogg, G.M., eds., The Geologic Time Scale 2012, Elsevier BV, p. 603–651, https://doi.org/10.1016/B978-0-444-59425-9.00023-8.

Davydov, V., Schmitz, M.D., and Korn, D., 2011, The Hangenberg Event was abrupt and short at the global scale; the quantitative intergration and intercalibration of biotic and geochronologic data within the Devonian-Carboniferous transition: Geological Society of America Abstracts with Programs, v. 43, no. 5, p. 128, https://gsa.confex.com/gsa/2011AM/webprogram/Paper195211.html.

De Vleeschouwer, D., Boulvain, F., Da Silva, A.-C., Pas, D., Labaye, C., and Claeys, P., 2014, The astronomical calibration of the Givetian (Middle Devonian) time scale (Dinant Synclinorium, Belgium): Geological Society of London, Special Publications, v. 414, p. 245–256, https://doi.org/10.1144/SP414.3.

De Vleeschouwer, D., Königshof, P., and Claeys, P., 2018, Reading time and paleoenvironmental change in the Emsian–Eifelian boundary GSSP section (Wetteldorf, Germany): A combination of cyclostratigraphy and facies analysis: Newsletters on Stratigraphy, v. 51, p. 209–226, https://doi.org/10.1127/nos/2017/0397.

De Vleeschouwer, D., Whalen, M.T., Day, J.E., and Claeys, P., 2012, Cyclostratigraphic calibration of the Frasnian (Late Devonian) time scale (western Alberta, Canada): Geological Society of America Bulletin, v. 124, p. 928–942, https://doi.org/10.1130/B30547.1.

Ellwood, B.B., El Hassani, A., Tomkin, J.H., and Bultynck, P., 2015, A climate-driven model using time-series analysis of magnetic susceptibility (χ) datasets to represent a floating-point high-resolution geological timescale for the Middle Devonian Eifelian stage: Geological Society of London, Special Publications, v. 414, p. 209–223, https://doi.org/10.1144/SP414.4.

Ellwood, B.B., Tomkin, J.H., Hassani, A.E., Bultynck, P., Brett, C.E., Schindler, E., Feist, R., and Bartholomew, A.J., 2011, A climate-driven model and development of a floating point time scale for the entire Middle Devonian Givetian Stage: A test using magnetostratigraphy susceptibility as a climate proxy: Palaeogeography, Palaeoclimatology, Palaeoecology, v. 304, p. 85–95, https://doi.org/10.1016/j.palaeo.2010.10.014.

House, M.R., 1995, Devonian precessional and other signatures for establishing a Givetian timescale, in House, M.R. and Gale, A.S. eds., Orbital Forcing Timescales and Cyclostratigraphy: Geological Society Special Publication No. 85, p. 37–49, https://doi.org/10.1144/GSL.SP.1995.085.01.03.

Husson, J.M., Schoene, B., Bluher, S., and Maloof, A.C., 2016, Chemostratigraphic and U–Pb geochronologic constraints on carbon cycling across the Silurian–Devonian boundary: Earth and Planetary Science Letters, v. 436, p. 108–120, https://doi.org/10.1016/j.epsl.2015.11.044.

Kaufmann, B., Trapp, E., Mezger, K., and Weddige, K., 2005, Two new Emsian (Early Devonian) U–Pb zircon ages from volcanic rocks of the Rhenish Massif (Germany): implications for the Devonian time scale: Journal of the Geological Society, v. 162, p. 363–371, https://doi.org/10.1144/0016-764904-012.

Kaufmann, B., 2006, Calibrating the Devonian Time Scale: A synthesis of U–Pb ID–TIMS ages and conodont stratigraphy: Earth-Science Reviews, v. 76, p. 175 190, http://doi.org/10.1016/j.earscirev.2006.01.001.

Lanik, A., Over, D.J., Schmitz, M., and Kirchgasser, W.T., 2016, Testing the limits of chronostratigraphic resolution in the Appalachian Basin, Late Devonian (middle Frasnian), eastern North America: New U-Pb zircon dates for the Belpre Tephra suite: Geological Society of America Bulletin, v. 128, p. 1813–1821, https://doi.org/10.1130/B31408.1.

Ma, K., Hinnov, L.A., Zhang, X., and Gong, Y., 2020, Astronomical time calibration of the Upper Devonian Lali section, South China: Global and Planetary Change, v. 193, p. 103267, https://doi.org/10.1016/j.gloplacha.2020.103267.

Macdonald, F.A., Schmitz, M.D., Strauss, J.V., Halverson, G.P., Gibson, T.M., Eyster, A., Cox, G., Mamrol, P., and Crowley, J.L., 2018, Cryogenian of Yukon: Precambrian Research, v. 319, p. 114–143, https://doi.org/10.1016/j.precamres.2017.08.015.

McAdams, N.E.B., Schmitz, M.D., Kleffner, M.A., Verniers, J., Vandenbroucke, T.R.A., Ebert, J.R., and Cramer, B.D., 2017, A new, high-precision CA-ID-TIMS date for the 'Kalkberg' K-bentonite (Judds Falls Bentonite): Lethaia, v. 51, p. 344–356, https://doi.org/10.1111/let.12241.

Melchin, M.J., Sadler, P.M., and Cramer, B.D., 2020, Chapter 21 – The Silurian Period, in Gradstein, F.M., Ogg, J.G., Schmitz, M.D., and Ogg, G.M., eds., Geologic Time Scale 2020: Amsterdam, Netherlands, Elsevier, p. 695–732, https://doi.org/10.1016/B978-0-12-824360-2.00021-8.

Myrow, P.M., Ramezani, J., Hanson, A.E., Bowring, S.A., Racki, G., and Rakociński, M., 2014, High-precision U–Pb age and duration of the latest Devonian (Famennian) Hangenberg event, and its implications: Terra Nova, v. 26, p. 222–229, https://doi.org/10.1111/ter.12090.

Parry, S.F., Noble, S.R., Crowley, Q.G., and Wellman, C.H., 2011, A high-precision U–Pb age constraint on the Rhynie Chert Konservat-Lagerstätte: time scale and other implications: Journal of the Geological Society, v. 168, p. 863–872, https://doi.org/10.1144/0016-76492010-043.

Pas, D., Da Silva, A.-C., Over, D.J., Brett, C.E., Brandt, L., Over, J.-S., Hilgen, F.J., and Dekkers, M.J., 2021, Cyclostratigraphic calibration of the Eifelian Stage (Middle Devonian, Appalachian Basin, Western New York, USA): Geological Society of America Bulletin, v. 133, p. 277–286, https://doi.org/10.1130/B35589.1.

Pas, D., Hinnov, L., Day, J.E., Kodama, K., Sinnesael, M., and Liu, W., 2018, Cyclostratigraphic calibration of the Famennian stage (Late Devonian, Illinois Basin, USA): Earth and Planetary Science Letters, v. 488, p. 102–114, https://doi.org/10.1016/j.epsl.2018.02.010.

Percival, L.M.E., Davies, J.H.F.L., Schaltegger, U., De Vleeschouwer, D., Da Silva, A.-C., and Föllmi, K.B., 2018, Precisely dating the Frasnian–Famennian boundary: implications for the cause of the Late Devonian mass extinction: Scientific Reports, v. 8, p. 9578, https://doi.org/10.1038/s41598-018-27847-7.

R Core Team, 2021, R: A language and environment for statistical computing: Vienna, Austria, R Foundation for Statistical Computing, https://www.R-project.org/ (accessed July 2021).

Schaltegger, U., Schmitt, A.K., and Horstwood, M.S.A., 2015, U–Th–Pb zircon geochronology by ID-TIMS, SIMS, and laser ablation ICP-MS: Recipes, interpretations, and opportunities: Chemical Geology, v. 402, p. 89–110, https://doi.org/10.1016/j.chemgeo.2015.02.028.

Schmitz, M.D., 2012, Appendix 2 - Radiometric ages used in GTS2012, in Gradstein, F.M., Ogg, J.G., Schmitz, M.D., and Ogg, G.M., eds., The Geologic Time Scale 2012: Amsterdam, Netherlands, Elsevier BV, p. 1045–1082, https://doi.org/10.1016/B978-0-444-59425-9.15002-4.

Selby, D., and Creaser, R.A., 2005, Direct radiometric dating of the Devonian-Mississippian time-scale boundary using the Re-Os black shale geochronometer: Geology, v. 33, p. 545–548, https://doi.org/10.1130/G21324.1.

Sláma, J., et al., 2008, Plešovice zircon — A new natural reference material for U–Pb and Hf isotopic microanalysis: Chemical Geology, v. 249, p. 1–35, https://doi.org/10.1016/j.chemgeo.2007.11.005.

Tucker, R.D., Bradley, D.C., Ver Straeten, C.A., Harris, A.G., Ebert, J.R., and McCutcheon, S.R., 1998, New U–Pb zircon ages and the duration and division of Devonian time: Earth and Planetary Science Letters, v. 158, p. 175 186, 10.1016/s0012-821x(98)00050-8.

Turgeon, S.C., Creaser, R.A., and Algeo, T.J., 2007, Re–Os depositional ages and seawater Os estimates for the Frasnian–Famennian boundary: Implications for weathering rates, land plant evolution, and extinction mechanisms: Earth and Planetary Science Letters, v. 261, p. 649–661, https://doi.org/10.1016/j.epsl.2007.07.031.

Wellman, C.H., 2004, Palaeoecology and palaeophytogeography of the Rhynie chert plants: evidence from integrated analysis of in situ and dispersed spores: Proceedings of the Royal Society of London. Series B, Biological Sciences, v. 271, p. 985–992, https://doi.org/10.1098/rspb.2004.2686.

Whalen, M.T., De Vleeschouwer, D., Payne, J.H., Day, J.E., Over, D.J., and Claeys, P., 2016, Pattern and timing of the Late Devonian biotic crisis in western Canada: Insights from carbon isotopes and astronomical calibration of magnetic susceptibility data, in Playton, T.E., Kerans, C., and Weissenberger, J.A.W., eds., New Advances in Devonian Carbonates: Outcrop Analogs, Reservoirs, and Chronostratigraphy, SEPM Special Publication No. 107, p. 185–201, http://doi.org/10.2110/sepmsp.107.02.